


Rifting of Extensional Flows on a Sphere

Roiy Sayag¹,^{*},[†]*Department of Environmental Physics, Blaustein Institutes for Desert Research, Ben-Gurion University of the Negev, Sede Boqer Campus, 8499000, Israel* (Received 19 April 2019; published 19 November 2019)

The front of a fluid that displaces a less viscous fluid in shear-dominated flows is known to be stable. We show that in predominantly extensional flows on a sphere, a similar front of a strain-rate-softening fluid can become unstable and evolve fingerlike patterns comprised of rifts and tongues. The number of rifts and tongues declines with time and is selected by competition between interfacial hoop stress, geometric stretching, momentum dissipation, and spatial curvature. Our results elucidate fracture dynamics in complex fluids under extension and are applicable to a wide range of systems, including planetary-scale ice shelves as in snowball epochs and icy moons.

DOI: 10.1103/PhysRevLett.123.214502

Instability of the moving interface of a fluid that displaces another fluid in a quasitwo dimensional geometry is a fundamental problem in a range of phenomena. Numerous studies have addressed the case where the flow is shear dominated [1–9] and analogous to flow within a gap between two solid surfaces (Hele-Shaw cell). When the gap is uniform, the interface of a more viscous displacing fluid is known to be stable [10]. Similar flows over a solid plane and with a free surface, as in viscous gravity currents, are also dominated by shear and have stable interfaces [11–13]. However, when traction is absent from both the top and bottom fluid surfaces, the flow becomes predominantly extensional and the evolution of the interface can change radically. In particular, an initially circular interface of a strain-rate-softening fluid displacing an inviscid fluid in a planar geometry can develop tearing patterns with sharp tips (Fig. 1), separated by a number of tongues [14]. Over time, the number of tongues declines by the joining of adjacent tongues into wider ones and the simultaneous relief of the tears' propagation. Such an instability is not observed when the displacing fluid is Newtonian [15,16].

This tearing instability is of prime importance to the understanding of fracture dynamics in complex fluids under extension. It may also be important to the understanding of the formation and evolution of ice rifts, which are fractures that split the fronts of ice shelves across their entire thickness [17]. Glacier ice deforms viscously over the bedrock like a strain-rate-softening fluid [18] and can spread across the grounding line into the oceans as a floating ice shelf. When not confined by lateral boundaries, the spreading is predominantly extensional and the ice shelf can split into a number of tongues separated by rifts [19]. Such rifts extend the ice-ocean interface where melting occurs and may trigger calving of icebergs [20] and possibly disintegration of ice shelves [21], which are the main mechanisms of mass loss in Antarctica [22]. On a

planar geometry, the tearing instability is driven by hoop stresses and inhibited by geometric stretching and momentum dissipation [23]. However, the presence of extensional

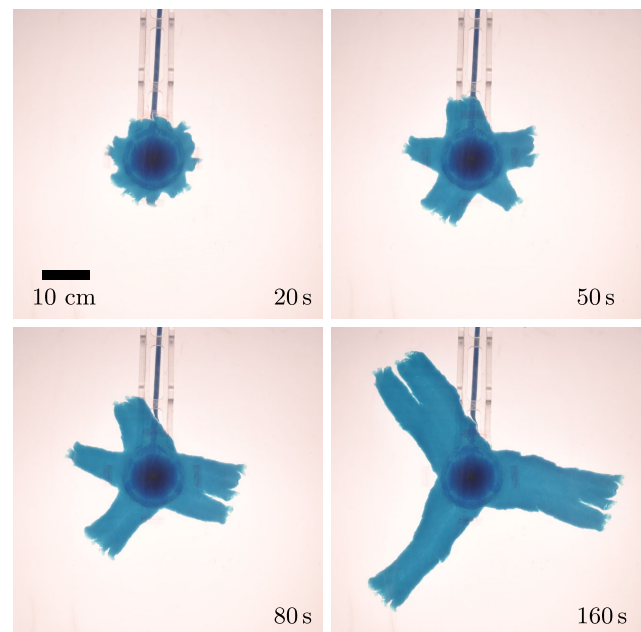


FIG. 1. Snapshots (plan view) from a laboratory experiment in *planar geometry*, in which aqueous solution of Xanthan gum (blue) was discharged axisymmetrically and at constant flux into a tank that contained a deep layer of salt solution (transparent) [14]. The Xanthan solution was completely floating while displacing the denser salt solution. It was also substantially more viscous than the salt solution ($\approx 10^5$ times more viscous at zero strain rate), resulting in a nearly zero traction along the bottom interface of the displacing Xanthan solution, and consequently in an extensionally dominated stress field in the displacing fluid. The time sequence shows that the fluid-fluid interface evolved from a high number of tears and tongues to a lower number.

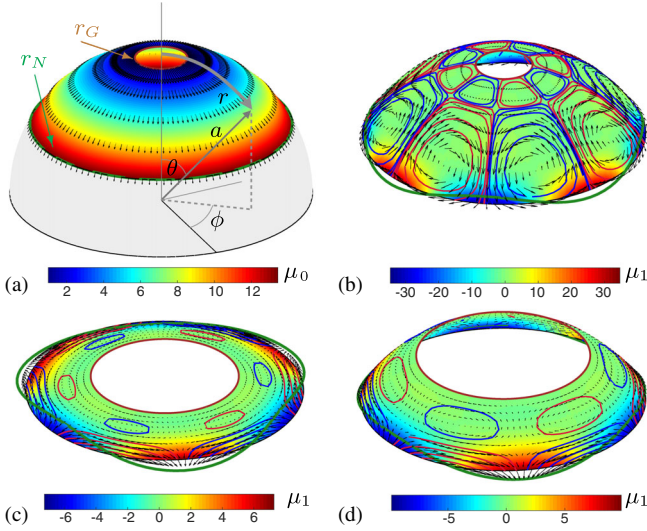


FIG. 2. (a) The spherical-cup geometry under consideration, together with the annular flow domain bounded between the inner geodesic distance r_G (brown solid line) and the outer one r_N (Green solid line), showing the base-state flow field (arrows) and viscosity μ_0 (color) for $n = 3$, $\theta_G = 10^\circ$, and $\theta_N = 60^\circ$. (b)–(d) The secondary flow velocity (arrows), streamlines (lines), and viscosity μ_1 (color) for a stable mode $k = 4$ with $\theta_G = 10^\circ$, $\theta_N = 60^\circ$ (b), and for two unstable modes with $k = 3$ and $\theta_G = 10^\circ$, $\theta_N = 19^\circ$ (c) and $\theta_G = 30^\circ$, $\theta_N = 55^\circ$ (d).

flows in nonplanar geometries, such as ice shelves on a planetary scale, raises the question of whether spatial curvature can inhibit the tearing instability or modify it. For example, during snowball epochs [24] ice caps covered Earth’s surface completely or excluding an equatorial ocean and challenged the survival of photosynthetic life [25–27]. Icy moons such as Europa and Enceladus have oceans covered by ice shells [28], which appear active in forming rifts, as implied from evidence of atmospheric water-vapor plumes [29] and elongated surface terrain [30]. Therefore, the scope of implications that rift patterns may have on a planetary scale could be wide and of prime interest, yet the role of spatial curvature on the stability of extensional flows remains unexplored thus far.

We explore the impact of spatial curvature by considering the stability of extensional flows on a sphere. The flow is of a thin, annular cap of power-law fluid that deforms without traction along its boundaries. The fluid cap of uniform thickness h is centered at the north pole of a sphere of radius $a \gg h$, that has horizontal coordinates ϕ for longitude and $r = a\theta$ for the geodesic distance from the north pole, where $0 \leq \theta \leq \pi/2$ is the latitude [Fig. 2(a)]. Therefore, in the limit of zero mean curvature ($a^{-1} \rightarrow 0$) the annular spherical cap converges to an annular disk and the solution should converge to that of a planar geometry [23]. The annular fluid cap has a fixed inner arc at $r_G = a\theta_G$ and a moving outer arc $r_N(\phi, t) = a\theta_N(\phi, t)$. The fluid is discharged at r_G at

constant flux Q axisymmetrically with respect to the pole. This configuration is similar to flow in a spherical Hele-Shaw cell of small aspect ratio ($a \gg h$) [9], but with no-stress instead of no-slip boundary conditions along the walls of the cell. Consequently, to leading order the flow is uniform in the radial (locally vertical) direction and essentially takes place in the surface of a two-dimensional sphere. For low Reynolds number flow, we use the Stokes equations of motion

$$\nabla \cdot \boldsymbol{\sigma} = \mathbf{0}, \quad \nabla \cdot \mathbf{v} = 0, \quad (1)$$

where $\mathbf{v} = v\hat{\mathbf{r}} + u\hat{\boldsymbol{\phi}}$ is the plan velocity field with latitudinal ($\hat{\mathbf{r}} = \hat{\boldsymbol{\theta}}$) and azimuthal components v and u respectively, $\boldsymbol{\sigma} = -p\mathbf{I} + 2\mu\mathbf{e}$ is the full stress tensor, p is the pressure field, \mathbf{I} is the identity tensor, $\mathbf{e} = \frac{1}{2}(\nabla\mathbf{v} + \nabla\mathbf{v}^T)$ is the rate-of-strain tensor, and μ is the strain-rate-dependent viscosity of a power-law fluid

$$\mu = m \left(\frac{1}{2} \mathbf{e} : \mathbf{e} \right)^{\frac{1}{2}[1/n-1]}, \quad (2)$$

where m is a constant coefficient, and n is a constant exponent representing a strain-rate-softening (shear-thinning) fluid when $n > 1$, a strain-rate-hardening (shear-thickening) fluid when $0 < n < 1$, and a Newtonian fluid when $n = 1$. The boundary conditions at the inner boundary r_G of the annular cap are kinematic

$$v = \frac{Q}{2\pi h a \sin(r/a)}, \quad u = 0, \quad (3)$$

and at the outer boundary $r_N(\phi, t)$ the tangential and normal stresses are zero. Finally, the velocity of the fluid front equals the material velocity at that front

$$\frac{dr_N}{dt} = v(r_N). \quad (4)$$

The dimensionless form of this model (Supplemental Material [31]) involves only the exponent n and θ_G as dimensionless groups. This implies dynamical similarity among a range of spatiotemporal scales, and particularly between laboratory-scale experiments (Fig. 1, [14]) and rifts in ice shelves. The geodesic distance r is scaled with r_G , so that the annular cap dimensionless boundaries are at 1 and $R \equiv r_N/r_G$, implying that the dimensionless form of (4) is $dR/dt = v(R)$, where v is dimensionless.

We now consider the linear stability of small perturbations with respect to an axisymmetric base-state solution, denoted with the subscript 0

$$u_0 = 0, \quad v_0 = \frac{\theta_G}{\sin(\theta_G r)},$$

$$\mu_0 = \left(\theta_G^2 \frac{|\cot(\theta_G r)|}{\sin(\theta_G r)} \right)^{1/n-1}. \quad (5a)$$

Therefore, the base-flow latitudinal velocity decreases with r and consequently so does the base-flow rate of strain,

resulting in the growth of the base-flow viscosity of a strain-rate-softening fluid ($n > 1$) with r [Fig. 2(a)]. The corresponding position of the base-flow front grows in time like

$$R_0 = \frac{1}{\theta_G} \cos^{-1}[\cos \theta_G - \theta_G^2 t]. \quad (5b)$$

Perturbations about the base flow (5), denoted with subscript 1, have the form

$$\mathbf{F} = \mathbf{F}_0(r) + \mathbf{F}_1(r, \phi, t), \quad (6a)$$

$$R = R_0(t) + R_1(\phi, t), \quad (6b)$$

where $\mathbf{F}_i \equiv (u_i, v_i, p_i, \mathbf{e}_i)$ for $i = 0, 1$. The geometric perturbation of the interface is $R_1 = \varepsilon e^{ik\phi + \mathcal{G}t}$, where $\varepsilon \ll 1$, k is an integer azimuthal wave number, \mathcal{G} is the growth rate, and \mathbf{F}_1/R_1 is function of r only, of order one. Substitution in the evolution equation for the front implies that the growth rate is

$$\mathcal{G} = \left(\frac{\partial v_0}{\partial r} + \frac{v_1}{R_1} \right) \Big|_{r=R_0} \quad (7)$$

to leading order. The first contribution is from the base-state stretching due to the curved geometry, which is always negative and therefore suppressing the perturbation growth independently of n and k . The second contribution from the secondary flow v_1/R_1 can be interpreted by combining the two boundary conditions of zero tangential and normal stresses at the leading front to

$$\frac{\partial \sigma_{1r\phi}}{\partial \phi}(R_0) = \frac{\theta_G}{\sin(\theta_G R_0)} \frac{\partial^2 R_1}{\partial \phi^2} \sigma_{0\phi\phi}(R_0), \quad (8)$$

which implies that the base-flow hoop stress $\sigma_{0\phi\phi}$ coupled with the perturbed geometry of the interface leads to a perturbation shear stress and consequently to a latitudinal force on the interface. Having $\sigma_{1r\phi} = \mu_0 e_{1r\phi}$, Eq. (8) can be solved for v_1 , implying (Supplemental Material [31]) that the growth rate (7) has the three contributions

$$\mathcal{G} = \frac{\partial v_0}{\partial r} + \frac{\sigma_{0\phi\phi}}{\mu_0} + \frac{\sin^2(\theta_G R_0)}{k^2 \theta_G^2 R_1} \frac{\partial}{\partial r} \left(\frac{\theta_G}{\sin(\theta_G r)} \frac{\partial u_1}{\partial \phi} \right), \quad (9)$$

representing, respectively, the stabilizing geometric stretching, the destabilizing hoop stress, and momentum dissipation. Among these three contributions only the latter depends on the wave number k and the fluid exponent n . We obtain the full solution to the growth rate by solving (1) to order ε (Supplemental Material [31]) for a range of n, k, R_0 and θ_G [e.g., Figs. 2(b) through 2(d)]. Consequently for any fixed inner boundary θ_G , we find that unstable modes rise only for strain-rate-softening ($n > 1$) fluids [Fig. 3(a)]. In addition, among the unstable modes

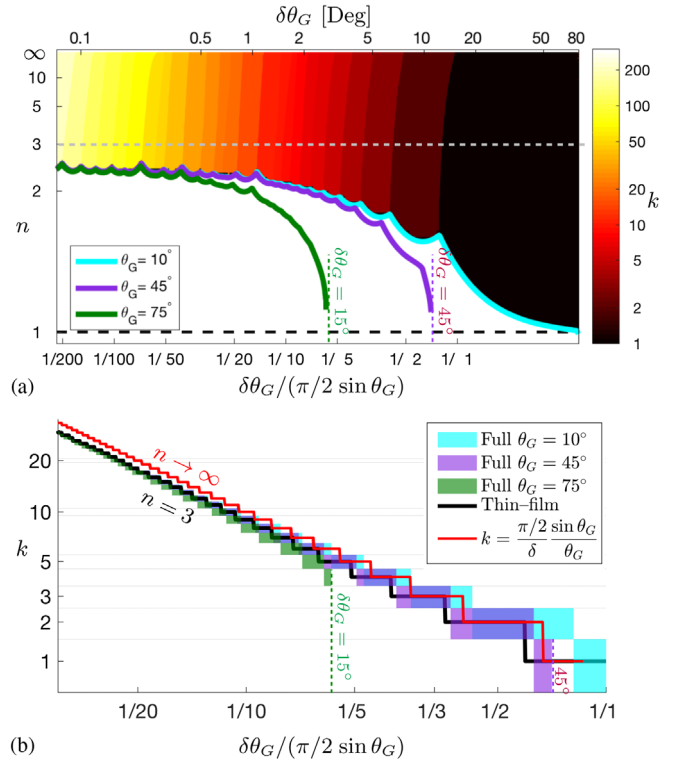


FIG. 3. (a) State-space diagram of the most-unstable wave numbers (color) for any n and width of the spherical cap (top axis) between $\theta_G = 10^\circ$ to $\theta_N = 90^\circ$, obtained from the full perturbation model. The neutral-stability curves for $\theta_G = 10^\circ$ (cyan line), 45° (purple line), and 75° (green line) are shown with respect to a normalized width (bottom axis) based on the plastic limit (12b). (b) The most unstable wave numbers for all cap width and for $n = 3$ [gray dashed line in (a)], computed by the full model for $\theta_G = 10, 45, 75^\circ$, and compared with the prediction of the thin-film approximation based on (11) (black line) and in the plastic limit (12b) (red line). (See Supplemental Material [31].)

the most-unstable wave number depends weakly on n and declines monotonically with the width of the cap $\delta \equiv R_0 - 1$. Also, the most-unstable wave number at the equator $\theta_N = \pi/2$ grows with θ_G .

The weak dependence of the most-unstable wave number on n implies that it can be predicted to a good accuracy in the plastic limit $n \rightarrow \infty$. To achieve that we first obtain a closed-form solution of the growth rate in the limit $\delta \ll 1$ and $k\delta\theta_G/\sin\theta_G \sim 1$, in which the cap width is much smaller than its inner geodesic distance and the wave number is high. In this limit the full perturbation model simplifies to (Supplemental Material [31])

$$v_1^{iv} - \frac{2(2-n)}{n} K^2 v_1'' + K^4 v_1 = 0, \quad K \equiv k\delta \frac{\theta_G}{\sin\theta_G}, \quad (10a)$$

where prime is a derivative with respect to $\xi \equiv (r-1)/\delta$, together with the boundary conditions at the inner boundary $\xi = 0$

$$v_1 = v'_1 = 0, \quad (10b)$$

and at the outer boundary $\xi = 1$

$$v''_1 + K^2 v_1 = 4K^2 \theta_G^2 \frac{\cot \theta_G}{\sin \theta_G} R_1, \quad (10c)$$

$$v'''_1 = K^2 \left(\frac{4}{n} - 1 \right) v'_1.$$

Therefore, the growth rate has the closed form

$$\mathcal{G} = \theta_G^2 \frac{\cot \theta_G}{\sin \theta_G} \frac{(2n-1) \sin^2 \sqrt{\frac{n-1}{n}} K^2 - (n-1) \cosh^2 \frac{K}{\sqrt{n}}}{\sin^2 \sqrt{\frac{n-1}{n}} K^2 + (n-1) \cosh^2 \frac{K}{\sqrt{n}}}, \quad (11)$$

which becomes in the plastic limit

$$\mathcal{G}_{\text{plastic}} = -\theta_G^2 \frac{\cot \theta_G}{\sin \theta_G} \cos(2K), \quad (12a)$$

implying that the most-unstable wave number k_{plastic} is given in that limit by $2K = \pi$, so that

$$k_{\text{plastic}} = \frac{\pi/2 \sin \theta_G}{\delta \theta_G}. \quad (12b)$$

Although (12b) applies in the limit $\delta \ll 1$, $K \sim 1$, and $n \rightarrow \infty$, it predicts quite well the most-unstable wave numbers obtained by the full solution for any n and δ and θ_G [Fig. 3(b)].

The physical mechanism underlying the instability is fundamentally similar to that in polar geometry [23]. Specifically, the base-flow hoop stress at the interface interacts with the geometric perturbation of the interface to generate tangential stress at the front (8). The resulting perturbation shear stress drives flow that converges into bulges in the perturbed interface and diverges from interfacial troughs. This flow pattern leads to the growth of the geometric perturbation, which intensifies the converging flow, leading to the development of the initial bulges into tongues. While the instability is independent of the fluid exponent n and the wave number, the stabilizing momentum dissipation depends on both n and k . Specifically, at large wave numbers ($K \gg \pi/2$) an array of eddies stabilizes the flow [Fig. 2(b)], while at small wave numbers ($K \ll \pi/2$) long streamlines that stretch between troughs and bulges provide a long dissipation path [Figs. 2(c) and 2(d)]. For strain-rate-softening fluids, the dissipation weakens as $n > 1$ grows, allowing the instability to emerge. The instability can persist even when friction along the base of the annular cap is included, although the growth rate is increasingly suppressed with the growth of friction (Supplemental Material [31]).

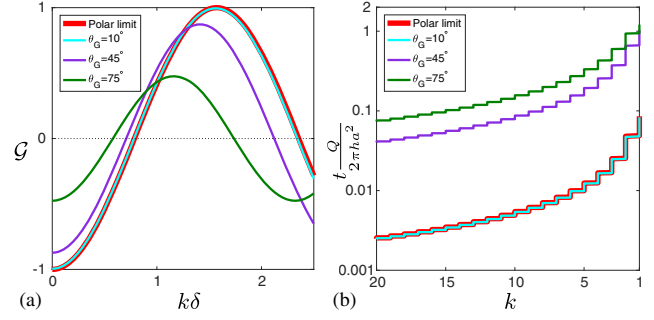


FIG. 4. The impact of spatial curvature on the instability is shown by (a) the plastic-limit growth rate (12a), and (b) the corresponding transition time to each mode k (12c) for $\theta_G = 10, 45, 75^\circ$, and compared with the prediction [23] of the zero-curvature limit $\theta_G \rightarrow 0$ (red line).

The curved geometry, represented by the mean spatial curvature a^{-1} or by θ_G in the dimensionless form, has two major impacts on the instability. The first is on the most-unstable wave number. Compared to planar geometry, the most-unstable wave number for a given width δ declines with the mean curvature like $\sin \theta_G / \theta_G$ (12b). Correspondingly, the growth rate of a specific mode k and width δ (12a) depends on both the mean curvature and the Gaussian curvatures θ_G^2 [Fig. 4(a)]. Consequently, the spatial curvature inhibits or triggers specific most-unstable modes, thereby modifying the resulted pattern of tongues. The second impact is on the transition time to a certain wave number. The predicted most-unstable wave number (12b) declines with the instantaneous annulus width δ , which grows with time (5b). This implies that the transition time to a wave number k is

$$t_{\text{plastic}} = 2\pi \frac{a^2 h}{Q} \left[\cos \frac{r_G}{a} - \cos \left(\frac{r_G}{a} + \frac{\pi/2 \sin \frac{r_G}{a}}{k} \right) \right] \quad (12c)$$

in dimensional form, and can change in curved geometry by more than factor 10 with respect to planar geometry [Fig. 4(b)]. We do not expect such a prediction to be valid in general at any finite time since it is based on a linear theory, whereas the experiments in the polar limit imply that the late-time evolution is highly nonlinear (Fig. 1). Nevertheless, the prediction corresponding to (12c) in the planar-geometry limit was found consistent with some experimental results [23]. Therefore, although based on a linear theory, (12c) may provide a good prediction of the transition time to the wave number k also at the presence of curved geometry.

As already mentioned, the model involves two dimensionless numbers representing the fluid exponent and the cap curvature. Therefore, the results above have implication to flows in a wide range of materials and spatiotemporal scales. One possible application is inhibiting or triggering tongue formation in complex fluids and controlling the time evolution of the fingering pattern by

modifying the spatial curvature, fluid properties, and the traction along the path of the flow. Another possible application is related to the dynamics of rifts in unconfined ice shelves. Predicting the evolution of rifts may lead to deeper understanding of how the length of the ice-ocean interface evolves and consequently the magnitude of glacier melting, and how rift formation and closure may trigger or inhibit iceberg calving. On a planetary scale ice sheets could have significantly larger unconfined shelves, implying that the impact of rifts could be on a much larger scale. Moreover, large spatial curvature implies that rifts would persist longer and that their number would decline more slowly. For example, in the last glacial maximum, the Antarctic grounding line was closer to circular [32], with potentially large unconfined ice shelves. Therefore, a grounding line at $r_G = 2500$ km and an unconfined ice shelf of width $\delta = 10$ km implies that 380 latitudinal rifts constitute the shelf (12b), making its front much longer than an otherwise smooth shelf. Therefore, accounting for rift formation may imply a significantly larger melting and possibly calving activity along the ice-ocean interface. In a snowball epoch, a likely thicker polar ice suggests that the flow within the ice caps was from high latitudes to low [33,34], implying an extensional ice flow where the ice is supported by an ocean. This suggests that latitudinal rifts could potentially form in a snowball ice sheet, and provide refuge pockets for living organisms that utilise sunlight. As indicated above, the decline in the number of rifts could slow down significantly due to the spatial curvature, which could increase the persistence of rifts as refuge pockets. Furthermore, in Europa it is conceivable that the ice flow over its ocean is latitudinal, from the poles towards the equator [35]. Although the resulted extensional flow is within a completely closed ice shell that could have important impact on the instability mechanism, it may still drive the formation of latitudinal rifts. Therefore, this mechanism may provide an alternative explanation to the observed water-vapor plumes and elongated terrain along the surface of icy moons.

Experimental validation of the results we present is challenging. The major difficulties rise due to the spherical geometry combined with the requirement to eliminate traction on the displacing fluid and avoid surface tension effects. While on plane geometry the issue of traction is resolved by using a less viscous ambient fluid of higher density [14], accomplishing such ambient conditions on spherical geometry without radial gravitational field is not trivial. Possible experimental approaches are to generate a gravity current over a sphere [36] with a constant source of polymer solution, or use a spherical Hele-Shaw cell. In both cases traction along the solid surfaces could be reduced using superhydrophobic surfaces [37] or perforated surfaces through which lubricating fluids are introduced.

I am grateful to Y. Ashkenazy, M. G. Worster, and B. Zaltzman for constructive feedback. This research was supported by the Israel Science Foundation (Grant No. 1368/16).

*roiy@bgu.ac.il; <http://www.bgu.ac.il/~roiy/>

†Also at Department of Mechanical engineering, Ben-Gurion University of the Negev.

- [1] L. Paterson, *J. Fluid Mech.* **113**, 513 (1981).
- [2] E. Lemaire, P. Levitz, G. Daccord, and H. Vandamme, *Phys. Rev. Lett.* **67**, 2009 (1991).
- [3] H. Zhao and J. V. Maher, *Phys. Rev. E* **47**, 4278 (1993).
- [4] B. Jha, L. Cueto-Felgueroso, and R. Juanes, *Phys. Rev. Lett.* **106**, 194502 (2011).
- [5] K. Bhaskar, P. Garik, B. Turner, J. Bradley, R. Bansil, H. Stanley, and J. Lamont, *Nature (London)* **360**, 458 (1992).
- [6] A. C. Callan-Jones, J. F. Joanny, and J. Prost, *Phys. Rev. Lett.* **100**, 258106 (2008).
- [7] D. Coumou, T. Driesner, S. Geiger, C. A. Heinrich, and S. Matthai, *Earth Planet. Sci. Lett.* **245**, 218 (2006).
- [8] T. T. Al-Housseiny, P. A. Tsai, and H. A. Stone, *Nat. Phys.* **8**, 747 (2012).
- [9] F. Parisio, F. Moraes, J. A. Miranda, and M. Widom, *Phys. Rev. E* **63**, 036307 (2001).
- [10] P. G. Saffman and G. Taylor, *Proc. R. Soc. A* **245**, 312 (1958).
- [11] H. E. Huppert, *J. Fluid Mech.* **121**, 43 (1982).
- [12] R. Sayag and M. G. Worster, *J. Fluid Mech.* **716**, R5 (2013).
- [13] K. N. Kowal and M. G. Worster, *J. Fluid Mech.* **871**, 1007 (2019).
- [14] R. Sayag and M. G. Worster, *J. Fluid Mech.* **881**, 722 (2019).
- [15] S. S. Pegler and M. G. Worster, *J. Fluid Mech.* **696**, 152 (2012).
- [16] R. Sayag, S. S. Pegler, and M. G. Worster, *Phys. Fluids* **24**, 091111 (2012).
- [17] T. Hughes, *J. Glaciol.* **29**, 98 (1983).
- [18] J. W. Glen, *Proc. R. Soc. A* **228**, 519 (1955).
- [19] H. Fricker, N. Young, R. Coleman, J. Bassis, and J. Minster, *Geophys. Res. Lett.* **32**, L02502 (2005).
- [20] D. I. Benn, C. R. Warren, and R. H. Mottram, *Earth Sci. Rev.* **82**, 143 (2007).
- [21] G. H. Gudmundsson, *Cryosphere* **7**, 647 (2013).
- [22] E. Rignot, S. Jacobs, J. Mouginot, and B. Scheuchl, *Science* **341**, 266 (2013).
- [23] R. Sayag and M. G. Worster, *J. Fluid Mech.* **881**, 739 (2019).
- [24] P. F. Hoffman, A. J. Kaufman, G. P. Halverson, and D. P. Schrag, *Science* **281**, 1342 (1998).
- [25] P. F. Hoffman and D. P. Schrag, *Terra nova* **14**, 129 (2002).
- [26] C. P. McKay, *Geophys. Res. Lett.* **27**, 2153 (2000).
- [27] A. J. Campbell, E. D. Waddington, and S. G. Warren, *Geophys. Res. Lett.* **38**, L19502 (2011).
- [28] M. G. Kivelson, K. K. Khurana, C. T. Russell, M. Volwerk, R. J. Walker, and C. Zimmer, *Science* **289**, 1340 (2000).
- [29] L. Roth, J. Saur, K. D. Retherford, D. F. Strobel, P. D. Feldman, M. A. McGrath, and F. Nimmo, *Science* **343**, 171 (2014).

- [30] R. T. Pappalardo *et al.*, *J. Geophys. Res. Planets* **104**, 24015 (1999).
- [31] See Supplemental Material at <http://link.aps.org/supplemental/10.1103/PhysRevLett.123.214502> for detailed description of the: (1) mathematical model; (2) stability analysis; (3) impact of basal friction on the stability; (4) instability mechanism; and of the (5) numerical solution.
- [32] N. R. Golledge, C. J. Fogwill, A. N. Mackintosh, and K. M. Buckley, *Proc. Natl. Acad. Sci. U.S.A.* **109**, 16052 (2012).
- [33] J. C. Goodman and R. T. Pierrehumbert, *J. Geophys. Res. Oceans* **108**, 3308 (2003).
- [34] E. Tziperman, D. S. Abbot, Y. Ashkenazy, H. Gildor, D. Pollard, C. G. Schoof, and D. P. Schrag, *J. Geophys. Res. Oceans* **117**, C05016 (2012).
- [35] Y. Ashkenazy, R. Sayag, and E. Tziperman, *Nat. Astron.* **2**, 43 (2018).
- [36] D. Takagi and H. E. Huppert, *J. Fluid Mech.* **647**, 221 (2010).
- [37] J. P. Rothstein, *Annu. Rev. Fluid Mech.* **42**, 89 (2010).